Experimental and Numerical Investigation of the Turbulent Wake Flow of a Generic Space Launcher Configuration

D. Saile, A. Gülhan
Institute of Aerodynamics and Flow Technology
German Aerospace Center, Linder Höhe, 51147 Köln, Germany

Abstract

The separated flow over a backward-facing step on a flat plate model is investigated at Mach 6 and a unit Reynolds number of $16 \cdot 10^6\,\mathrm{m}^{-1}$ in the hypersonic wind tunnel Cologne (H2K) by means of a microphone array supplemented by IR-thermography. Both measurement methods indicate reattaching counter-rotating vortices in the streamwise direction downstream of the backward-facing step most likely induced due to centrifugal instabilities. Information about the dynamic behavior and its spacial distribution in the recirculation region with distinct Strouhal numbers was acquired by means of the microphone array. Additional experiments were executed with sub-boundary layer disturbance elements just before the backward-facing step. It was shown that these elements result in a reattachment further upstream, and by changing the positioning of the elements, a systematic placement of the vortices was possible.

1. Introduction and Motivation

During the ascent trajectory of space transportation systems, some components of launchers are exposed to high thermal and mechanical and dynamic loads. Buffet, ground wind and base heat loads are some of the issues, which occur in different level of significance along the trajectory. Buffet is flow induced oscillation due to a separated flow and is most dominant in the transonic flow regime. Base heating is influenced by burning of the fuel-rich exhaust in the base region, by radiating exhaust gases and by recirculating flow downstream of the rear end of a rocket (Ref. [2]).

In previous studies (Ref. [8] and [9]), the flow around a space transportation system was simulated with generic axisymmetric elements consisting of a spherical nose, a cone and a cylinder (Fig. 1). Additionally, the influence of an external nozzle geometry was investigated by attaching another cylinder at the base. A backward-facing step (Fig. 2), referred to as BFS, is a subsequent step if the radius of the BFS is imagined to go to infinity while keeping the step height fixed.

A sketch of the mean flow features is given in Fig. 3. The incoming supersonic flow and the boundary layer on the surface of the model experiences an abrupt geometry change at the end of the model, which results in a flow separation. The separated flow expands and deviates consequently towards the lower flat plate. A free shear layer evolving right from the edge of the base separates the inviscid external flow from the recirculation region downstream of the base. The shear layer is subjected to an adverse pressure gradient before reattaching on the solid surface, whereas the flow consequently realigns along lower flat plate. This is where compression waves emanate and focus to a recompression shock.

Figure 1: Axisymmetric wind tunnel model

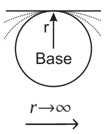

Figure 2: Backward-facing step

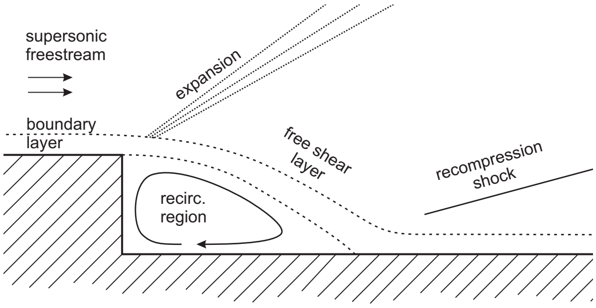

Figure 3: Schematic of the mean flow topology downstream of a BFS

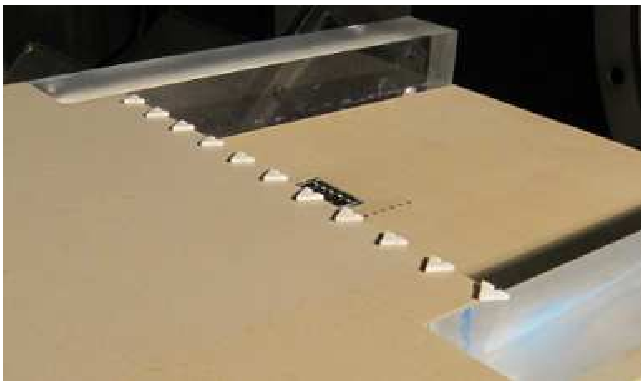

Figure 4: Sub-boundary layer disturbance elements at the end of upper flat plate

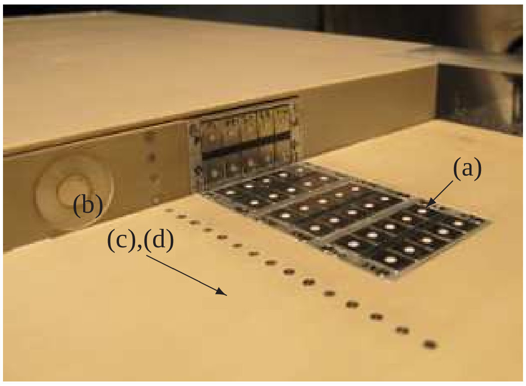

Figure 5: View on the instrumentation of the backward-facing step and lower flat plate

The objective of the paper is to present the behavior of the flow downstream of a BFS for conditions that equal a space transportation system at an altitude of approx. 50 km. IR-thermography and a microphone array were used as supplementing measurement methods with the intention to deduce mutually supporting conclusions about the flow topology downstream of the BFS, and additionally, investigate the periodicity of the unsteady recirculation region.

2. Experimental Facility, Measurement Methods and Analysis Methods

The measurements were performed in the supersonic, blow-down type wind tunnel H2K at the *Institute of Aerodynamics and Flow Technology* in the *Supersonic and Hypersonic Technology Department* located in Cologne. The H2K facility was operated at Mach 6.0 with a reservoir pressure and temperature of 18 bar and 470 K, which results in a unit Reynolds number of $16 \cdot 10^6\,\mathrm{m}^{-1}$. In order to show the influence of the Reynolds number, an exception was made for one set of experiments, where the reservoir pressure and temperature was set to 8 bar and 580 K leading to $Re = 5.1 \cdot 10^6\,\mathrm{m}^{-1}$.

The BFS features an overall length of 553 mm and a width of 300 mm. The upper flat plate length and the step height are 333 mm and 33 mm, respectively. For the $Re = 5.1 \cdot 10^6\,\mathrm{m}^{-1}$ case, a step height of 10.7 mm was realized. In order to limit three-dimensional side-effects, the lower plate is enclosed by side walls and, thus has a width of 220 mm. The investigated surfaces of the model are all made of PEEK. Carborundum with a grain size of 400 μm was applied on the tip to trigger transition to a turbulent boundary layer.

Additional experiments were executed with passive disturbances (Fig. 4) applied right before the edge of the BFS. These elements have an apex angle of 60°, a height of 1.5 mm and a length of 10 mm at the base. Since they were made of an existing zig-zag tape, they feature a gap with the same apex angle and a length of 2.5 mm at the base. The distribution between the elements was 27.5 mm.

The consecutively listed agreements are defined for the paper at hand. The origin of the coordinate system is located on the lower flat plate as the cross section between the centerline of the lower flat plate and the BFS. The positive x-axis is the centerline of the lower flat plate and the y-axis points crosswise along the corner of the BFS in such a way that z-axis, which is perpendicular to $x-y$-plane, is positive in the direction towards the upper flat plate. The flow in the images or pictures always comes from the left side and goes to the right. The color code in IR-images always goes from blue being the lowest temperature to red being the highest. The pressure spectra are plotted over the

Strouhal number representing the non-dimensional frequency, which is defined as $Sr_D = fH/u_\infty$ with the frequency f, the height of the BFS H and the free stream velocity u_∞.

Various measurement methods were applied to characterize the flow of the BFS. Fig. 5 shows the rear view on the model with the integrated sensors. Static pressure tabs (c), Kulites pressure transducers (d) and two types of microphones (a), (b) are depicted. The paper at hand is limited on the results downstream of the BFS, and besides the results of the microphone array, only infrared measurements and oil-film visualization are presented.

The infrared images of lower flat plate were captured with a *ThermaCAM SC 3000* of *FLIR Systems*. In the frame of the work here, infrared images are only used supportive for a better understanding of the results of the microphone array. Oil film visualization was executed with a silicone fluid featuring a kinematic viscosity of $350\,\mathrm{mm}^2/\mathrm{s}$ and a fluorescent dye.

The microphone array (Fig. 5 (a)) is compiled of single subminiature condenser microphones of the type *1207A* produced by *RTI Tech*, which exhibit the following main features: flat frequency response from 30 Hz to 15 kHz, phase invariance from 50 Hz to 5 kHz, sensitivity of 40 dB(1V/Pa), scatter of sensitivity of ± 3 dB(1V/Pa). Due to the high scatter of sensitivity and to the challenges in a low pressure environment, a calibration was disregarded. Consequently, the pressure fluctuation was normalized with the p_{rms}-values whenever possible. Variables that describe the frequency f or the skewness are unaffected by sensitivity and calibration.

The arrays are placed on the surface of the BFS and on the lower flat plate, whereas the alignment of the array's sensitive areas is in the streamwise and crosswise direction of the mean flow. On the lower flat plate, the first microphone is located at $(x, y) = (5, 16.1)$ mm. The next five sensors in the streamwise direction are now located at $x = 14.4, 25.2, 34.6, 45.45, 54.8$ mm. Measured from the edge, the microphones are located at $Dz = 5.4, 14.6$ and 25.6 mm. In the y-direction, the sensitive area of the microphones are in a distance of $\Delta y = 5.6$ mm to each other.

Each microphone is connected to the audiointerface *24 I/O* of *MOTU* enabling data acquisition with a sampling frequency of 96 kHz and a resolution of 24 bits. The signals are transferred to a computer using the *MOTU* PCI Express card *PCIX-424*. The pressure fluctuation p' are analyzed here by investigating the probability distribution function (PDF), the skewness, the root mean square of the pressure fluctuations p'_{rms} and the power spectral density (PSD) according to Ref. [13]. All of these commonly used statistical analysis can be found in literature (e.g. Ref. [12], [11]).

For the PSD, a hanning window function was applied on blocks of 8192 low-pass filtered data samples and normalized with p'_{rms} with an overlap of 50%. Additionally, a map with the spacial distribution of the peak strength was created for selected frequencies. Here, the window size comprised 4096 samples. The peak strength is basically the ratio of each value of the PSD to a polynomial fit through the PSD excluding the peaks. The maps later depict the peak level as a multiple of 20 of the logarithmic ratio between the peak and the reference spectrum.

3. Measurement Results

This chapter starts with the results that concern the overall flow features, continues then with findings about the reattachment and then evaluates data acquired via the microphone arrays. A second part then discusses observations due to disturbance elements. Data of the microphones are analyzed towards their statistical and time-dependent properties and compared to the IR-images.

3.1 Flow downstream of a backward-facing step without disturbance elements

Fig. 6 shows the top view of an IR-image on the lower flat taken during an experiment with the reference parameters. A cold region just behind the step can be detected. This region extends downstream up to a wavy line where the temperature rises again. It is evident that this line concludes the recirculation region behind the BFS. The end closer to the wavy line is the starting point of structures, which are arranged side by side and stretched in the streamwise direction. The structures exhibit a temperature maximum shortly after the tip, which decreases then further downstream. In total, approximately 16 to 17 structures can be found between the side walls. In the center region, the pattern is completely two-dimensional, whereas the first two structures next to the wall feature a notable deviation towards the x-axis.

Longitudinal structures can also be detected in the oil film visualized images (Fig. 7) that is taken from a slightly different perspective and distance. Just behind the step, the oil film is still homogeneously distributed up to a distance downstream from the backward-facings step where longitudinal streaks of high oil concentration have formed. Roughly 16 lines formed by an oil film can be detected by eye. The two-dimensionality of the pattern itself is comparable to the IR-images in Fig. 6.

A closer look concerning the extension of the cold region is given in Fig. 8 for the unit Reynolds number $Re = 16 \cdot 10^6\,\mathrm{m}^{-1}$ and $5.1 \cdot 10^6\,\mathrm{m}^{-1}$ and a step height of $H = 33$ mm and 10.7 mm. The IR-images are plotted along with the root mean square values of the pressure fluctuations p_{rms} of the microphone signals. As a common denominator of the IR-images, one can observe that the wavy line is always located between $x/H = 1.5$ and 1.7 length step heights downstream of the BFS.

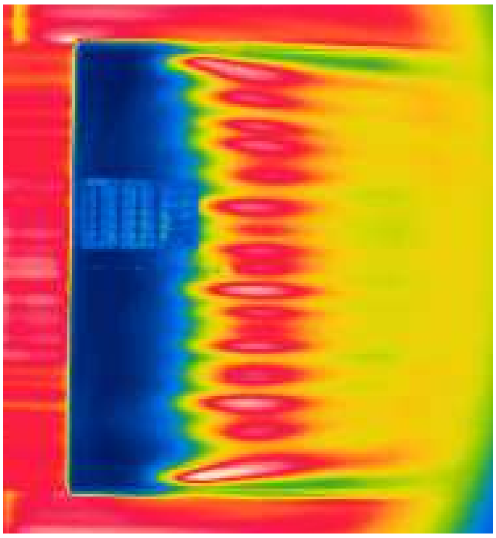

Figure 6: Top view of an infrared image showing the lower flat plate

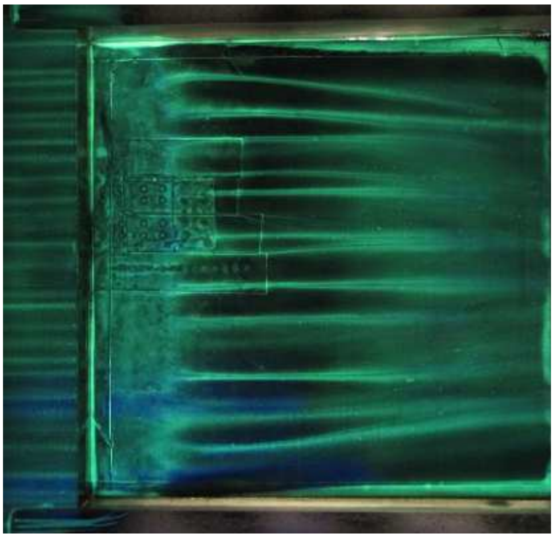

Figure 7: Top view on an image of the lower flat plate resulting from oil film visualization

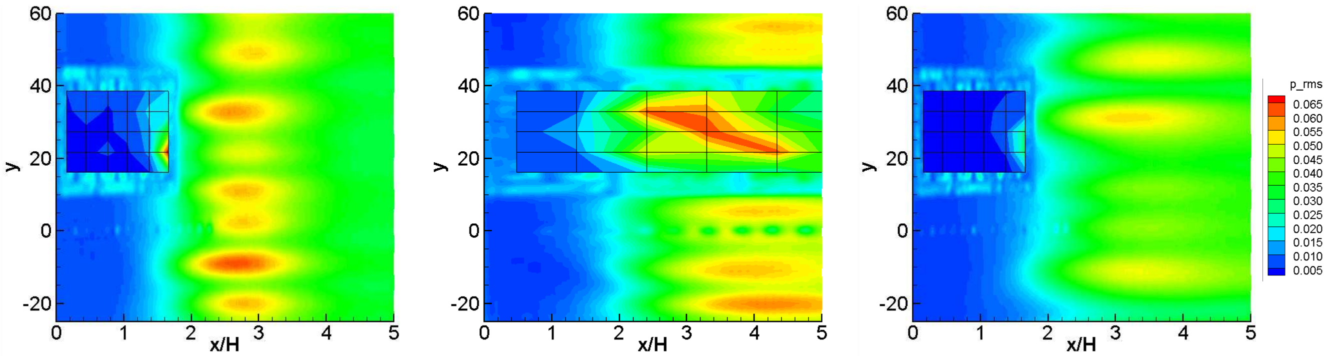

(a) $Re = 16 \cdot 10^6\,\mathrm{m}^{-1}$ and $H = 33\,\mathrm{mm}$ (b) $Re = 16 \cdot 10^6\,\mathrm{m}^{-1}$ and $H = 10.7\,\mathrm{mm}$ (c) $Re = 5.1 \cdot 10^6\,\mathrm{m}^{-1}$ and $H = 33\,\mathrm{mm}$

Figure 8: Top view on flat plate with joined measurement results from the microphone array and IR-thermography of the lower flat plate. Nodes on microphone array represent p_{rms}-values.

Further, Fig. 8(a), 8(b), 8(c) indicate a correlation between the wavy line of a temperature increase and the onset of larger magnitudes in p_{rms}-values. In the recirculation region, p_{rms}-values are low, then increase abruptly where the temperature is high, reach a maximum approximately where the temperature on the lower flat plate is the highest and decrease further downstream.

As it can be seen in Fig. 9, the microphones also acquired data of the flow dynamics on the BFS. In comparison to the neighboring microphones, the microphone closest to the centerline at a height $z = 18.4\,\mathrm{mm}$ ($\Delta z = 14.6\,\mathrm{mm}$) shows a high skewness that first decreases in the y-direction and increases again for the last microphone in that line. The same trend concerning the spanwise periodicity is notable for the line of microphones in the row closer to the edge and closer to the corner of the BFS.

The temporal periodicity can be extracted from Fig. 10. It shows the PSD of the microphones located at the center position of the array in the downstream direction (at $y = 26.1$mm), whereas the curves in the blue and brown color shade represent the signals from the BFS and the lower flat plate, respectively. In order to draw comparisons, each curve features a separate origin on the ordinate that is marked with a line of the corresponding color. The ticks indicate an increase of 0.125 of the power spectral density. The microphones within the recirculation region show a spacial dependence concerning the excitement of dominant Strouhal numbers. The spectra of the microphones in the reattachment region instead, starting at $x/H = 1.66$, depict no distinct peaks. The spectra are flat with a broad low-frequency pressure peak centering at about 0.01. This broad peak is generally also exhibited in the PSD of the microphones within the recirculation region.

Inside the recirculation region, peaks occur at about $Sr_H = 0.034, 0.062, 0.12, 0.19, 0.21, 0.246, 0.254, 0.291, 0.33, 0.455, 0.495$. The most prominent peaks can be found at the $x/H = 0.76$ at $Sr_H = 0.19, 0.21, 0.246, 0.254$, and also in a less pronounced manner further downstream at $x = 1.05$ and, for $Sr_H = 0.254$ further upstream at

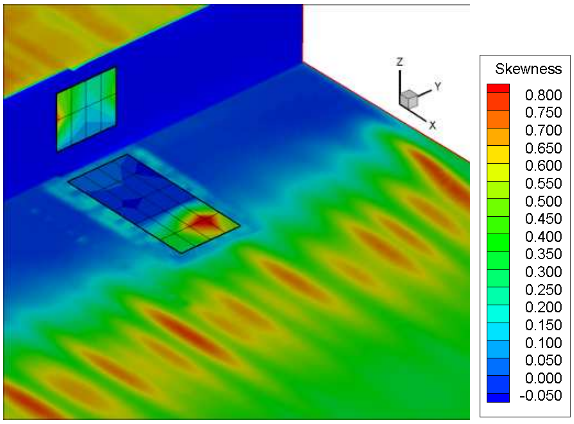

Figure 9: Joined measurement results showing an IR-image and the skewness of the PDF for each microphone

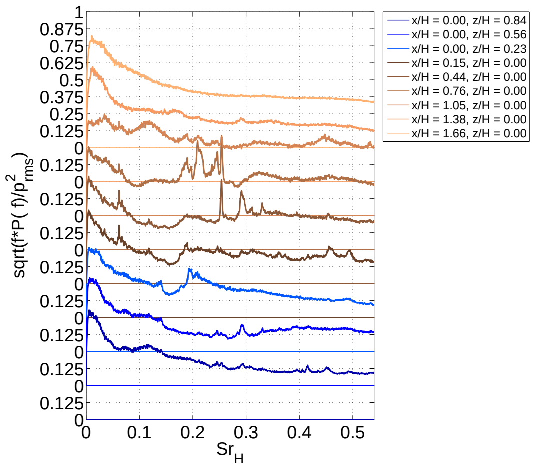

Figure 10: PSD of the microphones along the centerline of the array (at $y = 26.1$mm)

$x = 0.44$. The non-dimensional frequency at about $Sr_H = 0.19$ continuously exists on the lower flat plate as long the flow is not attached and also for the first microphone on the BFS at $z/H = 0.23$. Another commonly non-dimensional frequency appearing on the lower flat plate fluctuates with $Sr_H = 0.062$.

3.2 Influence of disturbance elements

One of the main goals for technical applications concerns the advantageous manipulation of the pressure and pressure fluctuations in the recirculation zone and the reattachment downstream of the BFS. A first step in this direction was taken by introducing the triangular shaped sub-boundary layer disturbance elements (described in Chap. 2) with the intention to change the flow by generating streamwise vortices.

The distribution of the elements is based on the idea that the IR-image in Fig. 6 is showing 16 almost equally distributed periodic pattern on the surface of the lower flat plate between the two walls. The approach of equally distributed patterns results in a wave length of $\lambda = 13.75$ mm and the elements were separated at the end of the upper plate according to $2 \cdot \lambda$ for the experiments presented here. Relatively to the wind tunnel model, two different arrangements were realized: one arrangement with the first disturbance element on the x-axis and another one with the first disturbance element one wavelength λ off the x-axis. The first configuration is from now on referred to as config. 1, the latter as config. 2.

IR-images in combination with p_{rms}-values or the skewness of the PDF are given in Fig. 11 for the experiments for both configurations. It can be seen that the disturbance elements cause a major change, whereas the IR-images indicate that the shift of the disturbance elements only result in an corresponding shift concerning the location of the thermal footprint (e.g. Fig. 11(a) and 11(b)).

The thermal footprints are strictly orientated according to the disturbance elements in such a manner they can only be found at the location directly further downstream of a disturbance element or in the gap between two disturbance elements. The result is that the number of thermal footprints is according to the number of elements, thus comparable to the the number found for the case with no elements (e.g. Fig. 9). The pattern now resembles fingers of different lengths whereas the fingers occurring in the gap between two disturbance elements reaches way closer upstream to the BFS showing that the influence of reattachment of the flow extends to about $x/H = 0.6$. Downstream of a disturbance element instead, the first indications of the longitudinal footprint occur about at $x/H = 1.6$, what is comparable to the flow with no disturbance elements.

The p_{rms}-values and the skewness as a result of the microphones are shown in Fig. 11(a) and 11(c) for config. 1. Extrapolating the thermal footprint indicates that high p_{rms}-values correlate with the region where high temperatures are measured and decrease towards the sides and upstream to the BFS where the temperature on the surface is low. The skewness instead seems to have the highest values along the boundary of the of the thermal footprint. This observation is supported by the experiments for config. 2 (Fig. 11(b) and 11(d)). Again, the p_{rms}-values are the highest where the thermal footprint can be noticed and the skewness seems to be high along the boundaries.

The influence of the disturbance elements on the periodic behavior of the flow behind the step is shown in Fig. 12(a) and 12(b) (legend equivalent to Fig. 10). All PSDs show a broad-band pressure low-frequency fluctuation at about $Sr_H = 0.02$, and generally, concerning the amplitude, a decreasing course for higher frequencies. Fig. 12(a) shows distinct pressure peaks in the region that is according to the IR-images (e.g. Fig. 11(a)) associated with the

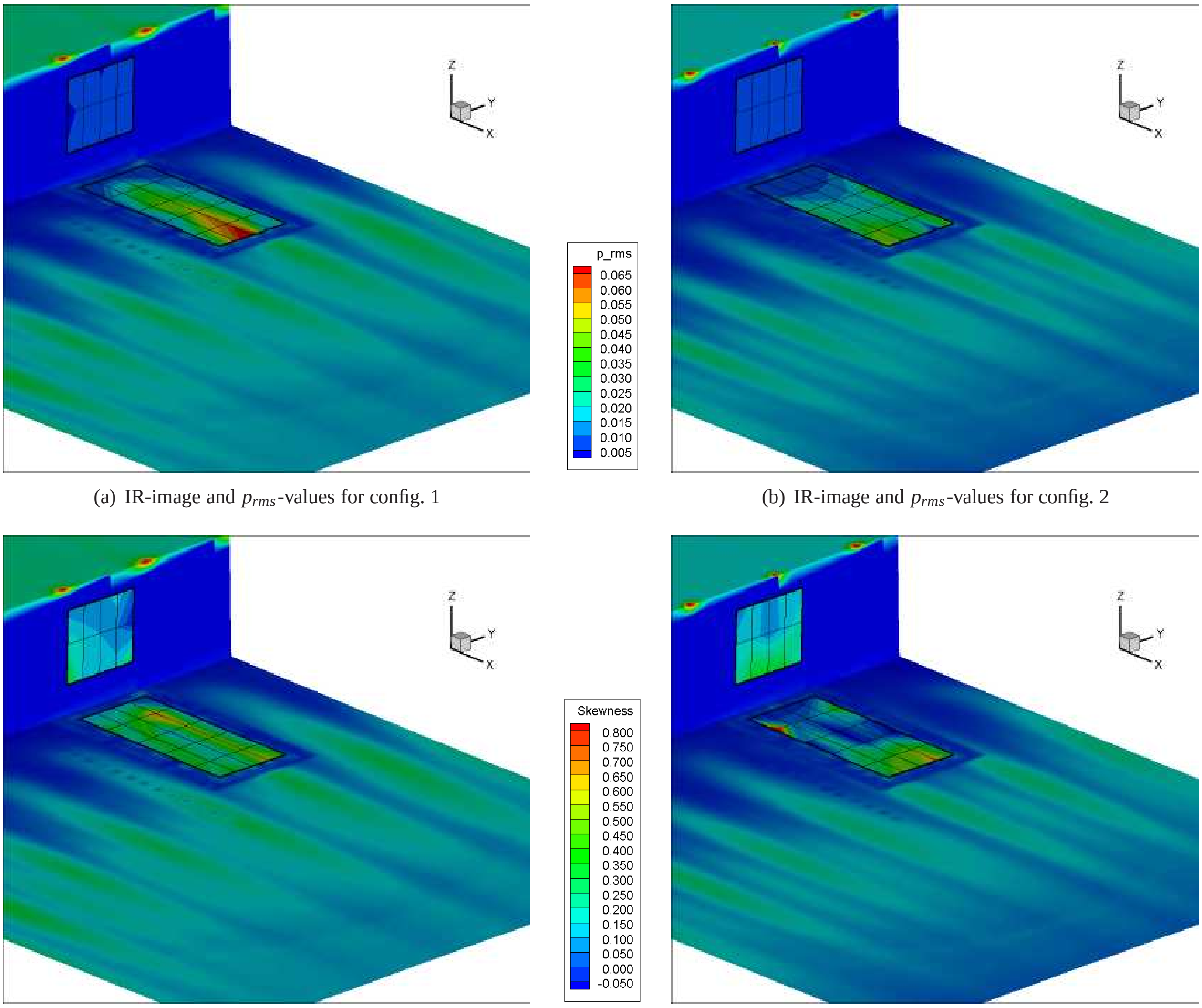

(a) IR-image and p_{rms}-values for config. 1

(b) IR-image and p_{rms}-values for config. 2

(c) IR-image and the skewness for config. 1

(d) IR-image and the skewness for config. 2

Figure 11: Isometric view showing the joined results from the microphone array and of IR-thermography for the case with disturbance elements

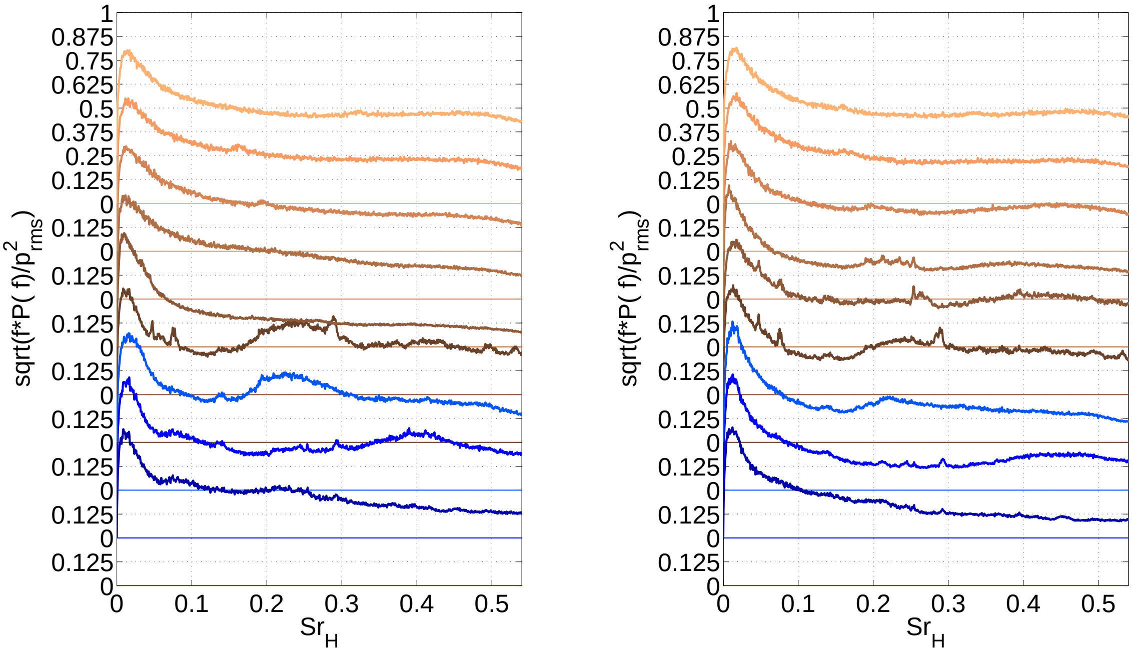

(a) Config. 1

(b) Config. 2

Figure 12: PSD of the microphones along the centerline of the array (at $y = 26.1$mm) for the case with disturbance elements

recirculation region. These pressure peaks occur at $Sr_H = 0.048, 0.074, 0.15, 0.254, 0.289$. The microphones in the reattachment region instead acquire a rather flat spectrum.

The spectra for the case with the shifted disturbance elements (Fig 12(b)) is similar close to the BFS. But, in comparison to the configuration before, the location where the microphones are excited periodically extends further downstream where additional non-dimensional frequencies can be observed at 0.19, 0.214, 0.232. Accordingly, the broad-banded flat spectra is also shifted further downstream. This observation correlates again with the IR-images. Notable is the location just before the reattachment at about $x/H = 0.76$ where Strouhal numbers of $Sr_H = 0.19$, 0.21, 0.254 can be discovered, which corresponds to the dominant frequencies found for the case with no disturbance elements (Fig. 10) just before at the location before reattachment takes place.

The areal distribution of the relative pressure peak strength for selected dominant Strouhal numbers are discussed in the following according to the method presented in Chap. 2 for both introduced configurations. A comparison for a Strouhal number of 0.232 (Fig. 13(a)) shows that high relative peaks can be observed on the BFS with two confined regions of moderate relative pressure peaks. The distance between the two regions constitutes approximately the distance of two microphones, which is 5.6 mm. On the lower flat plate higher relative peaks can be found close to the corner of the BFS, and, additionally for config. 2, a confined region of a high pressure peak level.

For a non-dimensional frequency of 0.254 (Fig. 13(b)), config. 2 exhibits a broad region of high relative peaks on the lower flat plate, which is detected by at least three to four microphones downstream of the BFS. For config. 1 instead, high relative peaks are only seen close to the corner of the BFS. On the BFS, both microphones signals feature high relative pressure peaks whereas these peaks are more extended in the vertical direction for config. 1.

4. Discussion of the Flow Topology, Driving Mechanisms and Oscillations

In the following, the flow downstream of the BFS is discussed in the order of occurrence concerning three-dimensionality, reattachment effects, periodicity of the recirculation/reattachment region and the spacial periodicity along the BFS by means of IR-thermography and the microphone array.

In order to deduce more general conclusions about the flow downstream of the BFS, it has to be ensured that the flow can be considered to be two-dimensional. The results of the IR-image (Fig. 6) and oil film visualization (Fig. 7) suggest that this is the case since only the first two structures show a notable deviation towards the centerline of the lower flat plate whereas the at least three-fourths of the lower flat plate including the area surrounding the microphone array are not influenced.

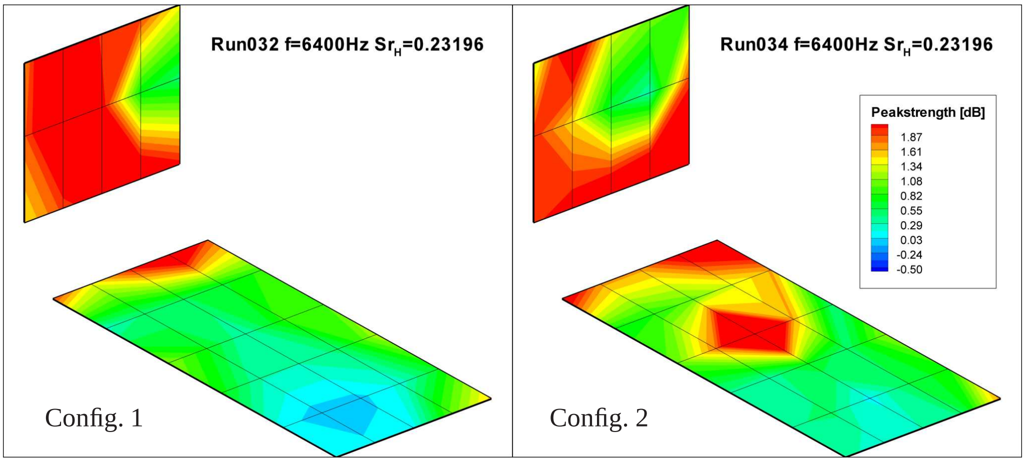

(a) Strouhal number $Sr_H = 0.232$

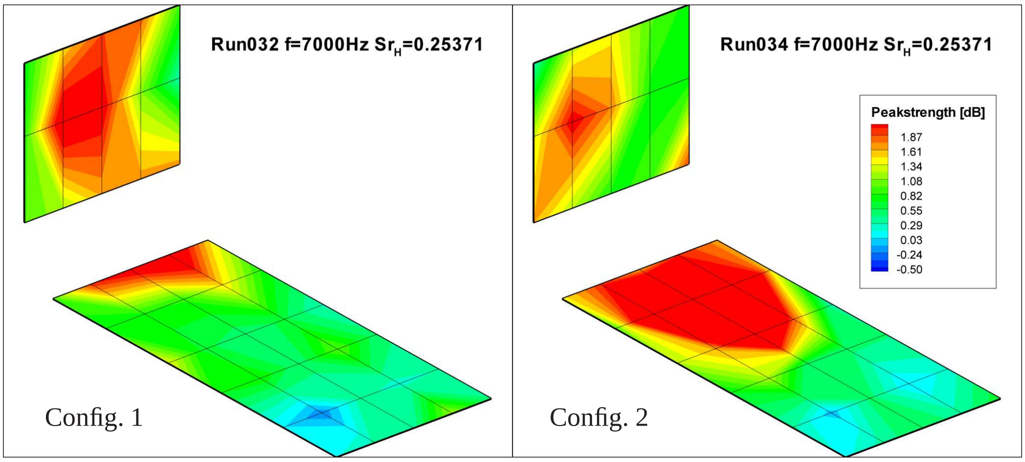

(b) Strouhal number $Sr_H = 0.254$

Figure 13: Areal distribution of the relative pressure peak strength

Information about the three-dimensional flow topology can be gathered by interpreting the IR-image in Fig. 6. The recirculation region is evidently marked by the restricted cold area just downstream of the BFS, which seems to scale with the step height H. Fig. 8(a) to 8(c) have shown that this region extends to about $x/H = 1.6 \pm 0.1$ downstream of the BFS and shows no sensitivity to the Reynolds number.

The reattachment of the flow is detectable by the structures stretched in the streamwise direction in IR-images. These structures can be interpreted as the thermal footprint of vortices, whereas fluid from the environment is transported onto and rises from the lower flat plate at the areas that show high and low thermal loads, respectively.

This statement is supported by the measurements using oil film visualization (Fig. 7), which is a measurement method for the shear stress on the surface. Within the recirculation region, the oil film is distributed homogeneously indicating a low level of shear stress. Downstream of the recirculation region, the oil film is collected in fine lines, which are also aligned in the streamwise direction. This indicates the location where the vortex causes an upward orientated flow and the downward transport of the fluid is located just in between to of these lines.

Looking at the IR-images, the projection of the vortex core on the lower flat plate is consequently located between the highest and the lowest temperature, and complementary for the oil film visualized images, two vortex cores a located somewhat elevated in the vertical direction between two lines of accumulated oil. Thus, each of the structure is caused by a pair of counter-rotating vortices. Helmholtz's second theorem states that a vortex filament cannot end in a fluid. It must extend to the boundaries or form a closed path. As a further consequence, the vortex core must either be connected upstream to the upper flat plate or to themselves. The curvature of the thermal footprint and the pattern of the shear stress induced dye path of the oil film visualization close to the BFS suggest that the cores of the counter-rotating vortices are connected.

For this reason, the reattachment of the flow cannot be considered to be a purely two-dimensional effect with a reattachment/stagnation line in the crosswise direction. Thus, two-dimensional numerical simulations do not capture the three-dimensional effects, and thus, are not sufficient. Instead, sets of connected counter-rotating vortices cause a stagnation lines in the streamwise direction. Additionally, these vortices impress a periodicity in the crosswise direction, which might be the driving mechanism for the azimuthal pressure distribution discovered by Ref. [5] for an axisymmetric configuration of a rocket with an attached nozzle.

The driving mechanism of the vortices is assigned to a centrifugal instability. The necessary and sufficient condition for the existence of inviscid axisymmetric instability is called Rayleigh circulation criterion [6], meaning the flow in a circular geometry is unstable if the ratio of the squared circulation Γ to the radius r is less equal then zero ($\partial(\Gamma^2)/\partial\ r < 0$). The instability results from an instable layering due to an induced local pressure gradient, which leads to an outward displacement. For an open system flow, like a fully-developed channel flow along a concave wall, this unstable flow is referred to as Dean instability or, in case of a boundary layer flow, it is called Görtler instability (Ref. [10]). Based on the two-dimensional results here, the vortices can not be clearly assigned to one of the instability mechanisms since no information is available in the third dimension to decide if the vortices are in- or outside of the boundary layer. Similar structures were observed downstream of the turbulent reattachment of an axisymmetric downstream-facing step (Ref. [7]) and downstream of a shock induced boundary layer separation (Ref. [3] and Ref. [4]).

Another explanation for the vortices might be that the vortices triggered upstream of the BFS by tripping elements at the tip of the model are maintained all the way downstream to the lower flat plate. This explanation is unlikely due to the fact that the number of vortices on the upper flat plate does not correlate with the ones on the lower flat plate further downstream. Another indication refers to the fact that the number of vortices on the lower flat plate is dependent on the step height.

Besides the IR- and oil visualized images, the microphone array also revealed interesting facts about the characteristics of the flow downstream of the BFS, which apply for the case with and without disturbance elements. The microphones have shown that the highest p_{rms}-values occur in the region where the reattachment takes place. This region is free from any distinct periodic excitement, which is shown in the rather flat frequency spectrum (Fig. 10, 12(a), 12(b)). At the boundaries between the recirculation region and the region where the flow is reattached, a high skew of the PDF can be noticed. Positive skew means that positive pressure peaks are more likely than negative. This might be caused due to an unsteady behavior of the vortices. According to [1], strong pressure drops correspond to vorticity concentration and generate a negative asymmetric probability density function. This holds true when the vortex causes a decreasing pressure along the surface. For the case at hand though, the reattaching flow is rather linked to an increasing pressure. And, if a wiggling vortex is imagined, then the microphone might be alternatively exposed to the flow of the reattachment and to the low-pressure of the recirculation region.

For the case with no disturbance elements (Fig. 10), this is also the region where the flow features the most distinct periodic excitement. Several dominant non-dimensional frequencies can be detected, e.g. at 0.19, 0.21, 0.246 and 0.254 among others. Closer to the corner of the BFS, some of these frequencies disappear and other frequencies are more present. Still existing is the Strouhal number of 0.19, but additionally a distinct peak at 0.12 is notable for several microphones.

The change of the base flow topology with disturbance elements is most evident when looking at the IR-images (Fig. 11(c) and 11(d)), which insinuate that they trigger streamwise vortices, and, thus force the flow to undergo a sharp deviation towards the lower flat plate. The vortex behind the disturbance elements remains approximately at the same location. These vortices react strictly to the location of the disturbance elements, and therefore they could be placed intentionally on the lower flat plate.

Besides the fact that the the disturbance elements crucially change the flow topology downstream of the BFS, the spectral analysis reveals that the flow is also slightly excited with a non-dimensional frequency of 0.19, 0.21, 0.246 and 0.254 right at the end of the recirculation region (Fig. 12). Another similarity can be found for the microphone closest to the corner that senses oscillations with a periodicity of about 0.29.

Noteworthy is that it seems like the periodicity of distinct fluctuations can directly be linked to the thermal footprint on the lower flat plate. The strong correlation is evident if the selected peak strength map for selected frequencies in Fig. 13(a) and 13(b) is compared with the IR-images (Fig. 11(c) and Fig. 11(d)). It seems obvious that the overall flow topology has an influence on the unsteady behavior of the recirculation region. But, the interpretation of the driving mechanisms and the interaction to the corresponding modes is not yet completely understood.

If the backward-facing step and the information from the microphone is considered now, it can be seen that the skewness seems to be a good indicator to deduce information about this region for the case without (Fig. 9) and with (Fig. 11(c) and Fig. 11(d)) disturbance elements. The skewness showed to locate the boundaries of vortices indicating a periodicity in the crosswise direction. For the case without disturbance elements, it seems like the acoustic footprint of two vortices can be detected. This interpretation can also be seen on the BFS for config. 1. The skew is high on the sides of the array. For config. 2 then, a higher skew is detectable in the center region of the array.

The observations about the skew have to be taken with care since a higher resolution is certainly desirable. But it seems like it is worthwhile following this path and take the skew as an indicator to determine the mean vortex structure downstream of the BFS and the mean location of vortices.

5. Conclusion

In the present work, the flow downstream of a backward-facing step (BFS) has been investigated for a Reynolds number of $16 \cdot 10^6\,\mathrm{m}^{-1}$ at Mach 6 in the hypersonic wind tunnel H2K. The investigations focused on the results of the microphone arrays, which were analyzed concerning the root mean square values, the skewness of the PDF and the spectral distribution of the fluctuations. These results were supplemented by IR-thermography.

As a first finding, the measurements revealed indications that the length of the reattachment region seems to scale with the step height, thus features a low sensitivity in the range of investigated Reynolds numbers. Further, IR-images and oil film visualization showed a highly three-dimensional flow field with patterns that are most likely caused by counter-rotating vortices in the streamwise direction induced by a centrifugal instabilities due to the convex curvature of the streamlines. The counter-rotating vortices and the resulting downward motion of the fluid are responsible for the generation of hot spots on the lower flat plate. Extrapolating these results and comparing them with the analyzed signals from the microphone array showed that the hot spots and the surrounding area correlate with high p_{rms}-values and the skew of the PDF, respectively. The microphones additionally disclosed the dominant fluctuations in the recirculation region. Besides other frequencies, the most distinct peaks were found for the cases without disturbance elements at $Sr_H = 0.19, 0.21, 0.246$ and 0.254 just before the end of the recirculation region. Less pronounced, these frequencies were also found for the case with disturbance elements at the same location. A mapping of the relative pressure peak level revealed that a correlation to the thermal footprint can be concluded for certain distinct frequencies.

On the one hand, the paper revealed that regions with high heat loads can be located and quantized. It is even possible to place these regions of high heat loads and take counteractive measures like protecting the surface of these regions with thermally high resistant materials. On the other hand, the knowledge about the exciting frequencies can be taken into account for the structural design base components.

The joined approach of the different measurement methods is seen as a key element in order to deduce more information about the physical properties of the flow. Following this approach, the next step intends to extend the available data from the surface bound measurement methods to the third dimension by using particle image velocimetry (PIV). The studies of influencing the flow downstream with passive methods will be continued and opportunities of active methods will be investigated.

Acknowledgement

Financial support by the German Research Foundation (Deutsche Forschungsgemeinschaft - DFG) in the framework of the Sonderforschungsbereich Transregio 40 is gratefully acknowledged. A data acquisition system has been kindly provided by the Institute of Aeronautics and Astronautics, RWTH Aachen. Thanks to Lars Koop from the Experimental Methods of the DLR in Göttingen for the gracious support, to Pascal Marquardt from the RWTH Aachen for his devoted work and to the technical stuff of the supersonic and hypersonic department for the excellent help.

References

[1] P. Abry, P. Fauve, P. Flandrin, and C. Laroche. Analysis of pressure fluctuations in swirling turbulent jets. *J. Phys. II France*, 4:407–416, 1994.

[2] R. W. Boswinkle. Aerodynamic problems of launch vehicles. *Aerodynamics of Space Vehicles, NASA SP-23*, pages 1–9, 1962.

[3] A. Henckels, A. Kreins, and F. Maurer. Experimental investigations of hypersonic shock-boundary layer interaction. *Z. Flugwiss. Weltraumforsch.*, 17:116–124, 1993.

[4] A. Henckels, A. Kreins, and F. Maurer. Experimental studies of hypersonic shock induced boundary layer separation. *Z. Flugwiss. Weltraumforsch.*, 20:80–88, 1996.

[5] J.-H. Meiss and W. Schröder. Large-eddy simulation of the base flow of a cylindrical space vehicle configuration. In *6th European Symopsium on Aerothermodynamics for Space Vehicles, ESA SP-659, Versaille, France*, 2009.

[6] Rayleigh. On the dynamcis of revolving fluids. *Scientific Papers*, 6:447–453, 1916.

[7] A. Roshko and G. Thomke. Observations of turbulent reattachment behind an axisymmetric downstream-facing step in supersonic flow. *AIAA Journal*, 4,6, 1966.

[8] D. Saile, A. Gülhan, and A. Henckels. Investigations on the near-wake region of a generic space launcher geometry. In *AIAA 2011-2352*, 2011.

[9] D. Saile, A. Gülhan, and A. Henckels. Investigations on the turbulent wake of a generic space launcher geometry in the hypersonic flow regime. In 4^{th} *European Conference for Aerospace Science*, 2011.

[10] W. S. Saric. Görtler vortices. *Ann. Rev. Fluid Mech.*, 26:379–409, 1994.

[11] H. Tennekes and J. L. Lumley. *A first Course in Turbulence*. MIT Press Desing Department, Fifteenth printing, ISBN 0262 200 19 8, 1994.

[12] W. H. P. S. A. Teukolsky, W. T. Vetterling, and B. P. Flannery. *Numerical Receipes*. Cambridge University Press, ISBN 978-0-521-88068-8, 2007.

[13] P. Welch. The use of fast fourier transform for the estimation of power spectra: a method based on time averaging over short, modified periodograms. *IEEE Transaction on Audio and Electroacoustics*, 15,2:70–73, 1967.